Viscoelastic control of spatiotemporal order in bacterial active matter

https://doi.org/10.1038/s41586-020-03168-6

Received: 26 September 2019

Accepted: 2 November 2020

Published online: 3 February 2021

Check for updates

Song Liu[1,6], Suraj Shankar[2,3,4,6], M. Cristina Marchetti[5] & Yilin Wu[1]✉

Active matter consists of units that generate mechanical work by consuming energy[1]. Examples include living systems (such as assemblies of bacteria[2–5] and biological tissues[6,7]), biopolymers driven by molecular motors[8–11] and suspensions of synthetic self-propelled particles[12–14]. A central goal is to understand and control the self-organization of active assemblies in space and time. Most active systems exhibit either spatial order mediated by interactions that coordinate the spatial structure and the motion of active agents[12,14,15] or the temporal synchronization of individual oscillatory dynamics[2]. The simultaneous control of spatial and temporal organization is more challenging and generally requires complex interactions, such as reaction–diffusion hierarchies[16] or genetically engineered cellular circuits[2]. Here we report a simple technique to simultaneously control the spatial and temporal self-organization of bacterial active matter. We confine dense active suspensions of *Escherichia coli* cells and manipulate a single macroscopic parameter—namely, the viscoelasticity of the suspending fluid— through the addition of purified genomic DNA. This reveals self-driven spatial and temporal organization in the form of a millimetre-scale rotating vortex with periodically oscillating global chirality of tunable frequency, reminiscent of a torsional pendulum. By combining experiments with an active-matter model, we explain this behaviour in terms of the interplay between active forcing and viscoelastic stress relaxation. Our findings provide insight into the influence of bacterial motile behaviour in complex fluids, which may be of interest in health- and ecology-related research, and demonstrate experimentally that rheological properties can be harnessed to control active-matter flows[17,18]. We envisage that our millimetre-scale, tunable, self-oscillating bacterial vortex may be coupled to actuation systems to act a 'clock generator' capable of providing timing signals for rhythmic locomotion of soft robots and for programmed microfluidic pumping[19], for example, by triggering the action of a shift register in soft-robotic logic devices[20].

Suspensions of swimming bacteria (bacterial active fluids) are important for bacterial dispersal and biofilm formation, and also offer a model system in which to study self-organization of active matter[5,21]. Concentrated bacterial suspensions display intriguing rheological properties not seen in equilibrium, such as vanishing apparent viscosity at low shear[3,22]. Although in nature most bacteria swim in viscoelastic fluids, the role of viscoelasticity on bacterial dynamics is largely unexplored experimentally, although it has been considered theoretically[23,24]. To examine whether fluid viscoelasticity modifies bacterial self-organization, we added purified genomic DNA from *E. coli* (~4.6 M base pairs, molecular weight ~3.0×10^9 Da) to dense suspensions of *E. coli* cells (0.8 μm in diameter, ~2–4 μm in length, swimming speed of ~20–40 μm s^{-1}) (Methods). *E. coli* DNA (hereinafter simply 'the DNA') was chosen because it has unusually high molecular weight and thus displays elastic response even at dilute concentrations[25]. This dense suspension of *E. coli* (~6×10^{10} cells ml^{-1}) was deposited on the surface of agar gel (Methods) to form a disk-shaped liquid drop (~1.5 mm in diameter and 20–30 μm in height at the centre; Fig. 1a and Extended Data Fig. 1a); the contact line of such a liquid drop remains stationary relative to the substrate.

When the DNA concentration was dilute, the bacterial suspension displayed a disordered state with small-scale collective motion of cells (a few tens of micrometres) in the form of transient vortices or jets[5], known as bacterial or mesoscale turbulence[4]. When the DNA concentration reached more than about 50 ng μl^{-1}, we observed that the entire bacterial suspension drop rotated either clockwise (CW) or counterclockwise (CCW) at a constant angular speed of ~0.1–0.15 rad s^{-1}, forming a millimetre-scale unidirectional vortex (Supplementary Video 1;

[1]Department of Physics and Shenzhen Research Institute, The Chinese University of Hong Kong, Hong Kong, P. R. China. [2]Department of Physics and Soft and Living Matter Program, Syracuse University, Syracuse, NY, USA. [3]Kavli Institute for Theoretical Physics, University of California, Santa Barbara, CA, USA. [4]Department of Physics, Harvard University, Cambridge, MA, USA. [5]Department of Physics, University of California, Santa Barbara, CA, USA. [6]These authors contributed equally: Song Liu, Suraj Shankar. ✉e-mail: ylwu@cuhk.edu.hk

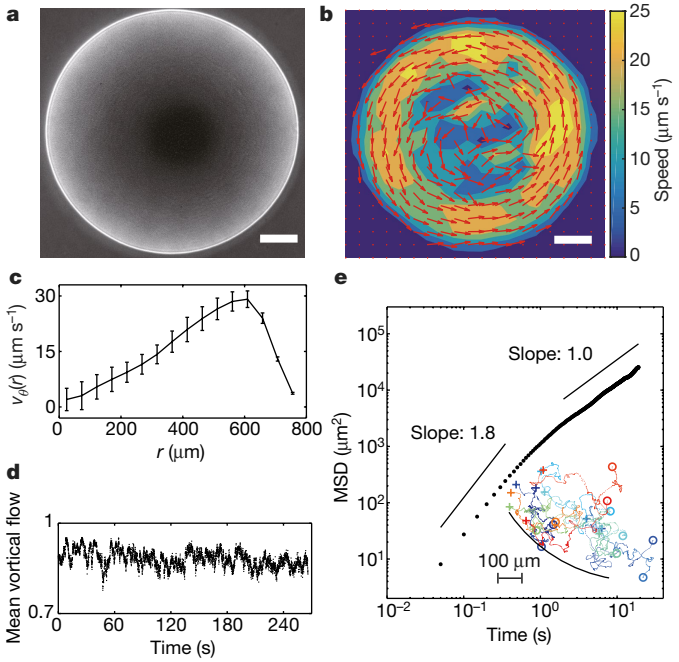

Fig. 1 | Unidirectional giant vortex. a, **b**, Phase-contrast image and instantaneous velocity field of a unidirectional giant vortex. Arrows and colourmap in **b** represent collective velocity direction and magnitude, respectively (Methods). DNA concentration, 200 ng μl^{-1}. Scale bars, 250 μm. Also see Supplementary Video 1. **c**, Time- and azimuthally averaged tangential velocity $v_\theta(r)$ of the giant vortex in **b** plotted against radial position. Error bars represent standard deviation (N = 1,000 successive frames). **d**, Normalized mean vortical flow of the giant vortex in **b** (Methods). **e**, Drift-corrected mean square displacement (MSD) of single cells in a giant vortex (Methods; Extended Data Fig. 2). Inset: trajectories of 11 representative cells (+, starting point; ○, ending point; dashed line, edge of suspension drop).

Extended Data Fig. 1b). To avoid confusion with the transient micro-scale vortices of bacterial turbulence, we refer to the millimetre-scale vortex observed here as a 'giant vortex'. The collective velocity vectors obtained by particle image velocimetry (PIV) were well aligned in the giant vortex (Fig. 1b), and the azimuthally averaged tangential velocity increased with distance from the vortex centre up to ~100–200 μm from the edge (Fig. 1c; Extended Data Fig. 1c). The normalized mean vortical flow (that is, tangential velocity averaged over the entire vortex; Methods) can also be used as an order parameter to characterize the vortex state, and it is indeed found to be near unity (Fig. 1d; Extended Data Fig. 1d). On average, bacteria moved in a coordinated way along the advective drift in the giant vortex, reflecting the collective transport of the suspension, since the ambient fluid is dragged along by the cells[5]. Tracking of individual trajectories also revealed local diffusive behaviour in a frame comoving with the vortex (Fig. 1e; Methods and Extended Data Fig. 2a, b). Previously, dense bacterial suspensions were reported to self-organize into stable vortices with coherent cell motion; such vortices had an upper size limit of ~100 μm, beyond which the collective motion became turbulent[21]. In contrast, the giant vortex observed here is an order of magnitude greater in size, showing that additive DNA aids large-scale spatial ordering of bacterial active fluids.

Strikingly, when the concentration of DNA was increased further (above about 300 ng μl^{-1}), the unidirectional giant vortex transitioned into an oscillatory state, in which the global rotational chirality switched between CW and CCW with a well defined period (Fig. 2a, b; Supplementary Videos 2–4). Meanwhile, individual bacteria still displayed local diffusive behaviour in a frame comoving with the vortex (Extended Data Fig. 2c). Numerical solution of the continuum active-matter model described below also reproduces the transition from coherent to oscillatory vortical flows (Fig. 2c, d and Supplementary Videos 5, 6). The oscillation dynamics of the giant vortex is clearly seen in the temporal evolution of the mean vortical flow (Fig. 2b) and of the tangential velocity profile along the radial direction (Fig. 2e, f). The period of chirality switching is accurate, with an error of less than ~20%, as revealed by Fourier spectrum analysis (Extended Data Fig. 1e–g). This switching period can be tuned by DNA concentration; it increased from ~10 s to ~50 s when the DNA concentration was increased from ~300 ng μl^{-1} to ~800 ng μl^{-1}.

Another important feature of the oscillatory giant vortex is that it acts like a relaxation oscillator[26]: the system transits quickly towards tangential (or angular) velocity extrema and progresses slowly away from the extrema, as manifested by the asymmetric shape of the velocity oscillation in Fig. 2f and by the parallelogram-like trajectory in the phase space of angular velocity and rotational angle (Fig. 2g). By contrast, the phase-space trajectory of a sinusoidal oscillation would have an elliptical shape.

We further examined the dynamics of global chirality switching of the giant vortex. At the initial stage of switching, a local vortex with opposite chirality tended to emerge near the periphery of the giant vortex (Fig. 3a). As the local vortex subsequently grew, a clear boundary with prominent local vorticity (referred to as the 'switching front') was formed (Fig. 3b; Methods). The space–time plot in Fig. 3c clearly shows the propagation of the switching front (Fig. 3d).

Cell density is an important control parameter for bacterial collective motion and self-organization[27]. We found that there exists a critical cell density of ~3 × 10^{10} cells ml^{-1} below which we could not observe the robust unidirectional giant vortex, nor the oscillatory one. At any cell density above this critical value, there existed two threshold DNA concentrations marking the onset of spatial order (unidirectional giant vortex) and temporal order (periodic switching of global rotational chirality of the giant vortex), denoted d_1 and d_2 respectively. Although the unidirectional giant vortex could be observed occasionally at DNA concentrations around 20–50 ng μl^{-1} (Extended Data Fig. 3; Methods), it only developed robustly at ~50 ng μl^{-1} for all cell densities, suggesting that d_1 remains fairly constant and can be approximately taken as ~50 ng μl^{-1}. We found that d_2 decreased from ~400 ng μl^{-1} to ~60 ng μl^{-1} as cell density increased from 4 × 10^{10} cells ml^{-1} to 8 × 10^{10} cells ml^{-1} (Fig. 4a). Moreover, as shown in the phase diagram of Fig. 4a, the chirality-switching frequency of the oscillatory giant vortex decreased with increasing cell density or DNA concentration over a sixfold tunable range between ~0.02 Hz and ~0.12 Hz; the tunable range is primarily controlled by DNA concentration and to a lesser extent by cell density. The amplitude of oscillations increased weakly with cell density and DNA concentration (Extended Data Fig. 4). These results demonstrate that, given sufficiently high cell density, additive DNA polymers regulate both spatial and temporal self-organization of bacterial active fluids.

To understand the mechanism underlying the self-organized oscillations, we model the bacterial suspension as an active polar bacterial fluid coupled to a viscoelastic solvent[11,18,28]. The local bacterial orientation is described by a polarization vector **p** coupled to the fluid flow velocity **v** and the elastic stress tensor $\sigma^{el} = 2G'\varepsilon$ of the DNA polymer, with G' the polymer storage modulus and ε the strain tensor. Assuming both the density of the suspension and the bacteria concentration to be constant, a minimal description of the active liquid crystal dynamics coupled to polymeric stress is given by

$$D_t\mathbf{p} + \Omega\mathbf{p} = \frac{1}{\gamma}\mathbf{h} + \lambda S\mathbf{p} - \frac{1}{\tau_R G'}\sigma^{el}\mathbf{p} \quad (1)$$

$$D_t\sigma^{el} + \Omega\sigma^{el} - \sigma^{el}\Omega = -\frac{1}{\tau_p}\sigma^{el} + 2G'S \quad (2)$$

with $D_t = \partial_t + \mathbf{v}\cdot\nabla$, $\Omega_{ij} = (\partial_i v_j - \partial_j v_i)/2$ the vorticity tensor and $S_{ij} = (\partial_i v_j + \partial_j v_i)/2$ the rate of strain tensor. The molecular field

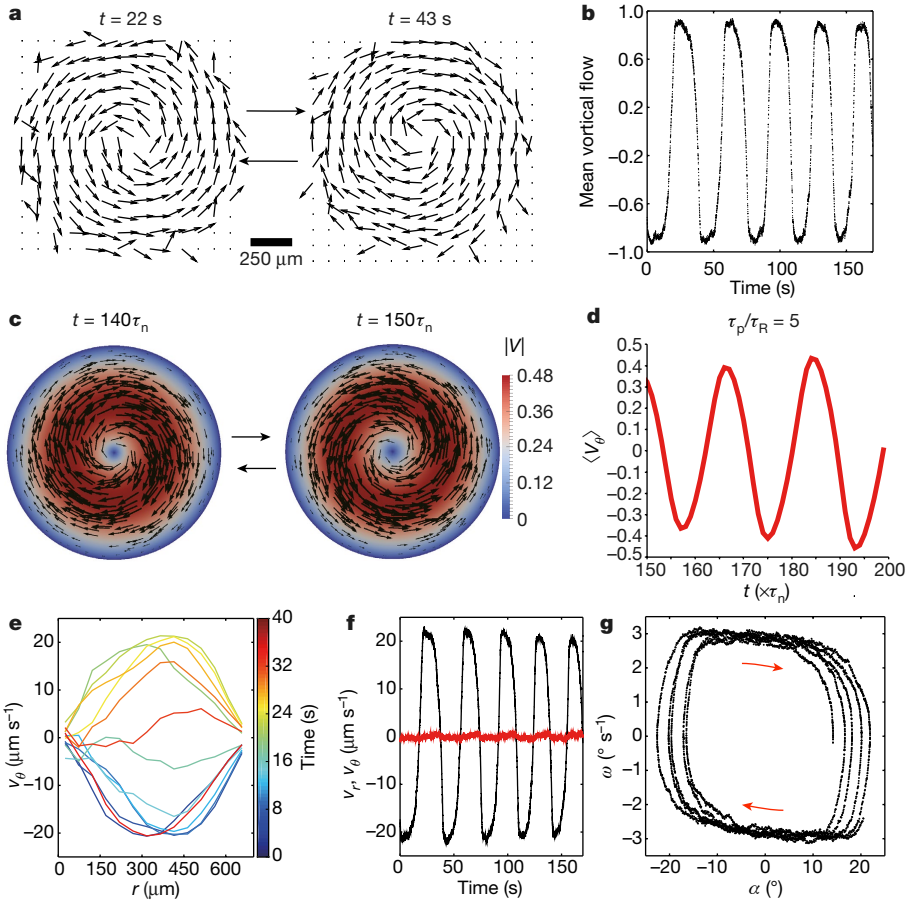

Fig. 2 | Oscillatory giant vortex. a, Two snapshots of the velocity direction field of an oscillatory giant vortex switching its global rotational chirality approximately every 35 s. DNA concentration, 800 ng μl^{-1}. **b**, Periodic chirality switching indicated by the oscillation of normalized mean vortical flow (positive, CCW; negative, CW). **c**, Two simulation snapshots showing periodic reversal of flow velocity. τ_n denotes the natural relaxation time of the bacteria orientation (Supplementary Information section I). Arrows and colourmap represent velocity direction and magnitude, respectively. **d**, Time trace of the mean vortical flow V_θ (Methods) associated with simulation results in **c**. **e**, Temporal evolution of azimuthally averaged tangential velocity v_θ during chirality switching. Colourmap indicates time. **f**, Time trace of azimuthally averaged tangential (v_θ; black) and radial (v_r; red) velocity computed near half radius of the giant vortex (390 μm ≤ r ≤ 440 μm). **g**, Phase-space trajectory of the oscillatory giant vortex in the plane of angular velocity ω and rotational angle α. ω is computed as v_θ/r in **f**, and α is computed by integrating ω over time. Also see Supplementary Videos 2–6.

$\mathbf{h} = [a(c - c_0) - b|\mathbf{p}|^2]\mathbf{p} + K\nabla^2\mathbf{p}$, with a, $b > 0$ and a single elastic constant K, yields a transition from a disordered ($|\mathbf{p}| = 0$) to a polar ordered state with $|\mathbf{p}| = p_0 = \sqrt{a(c - c_0)/b}$ at cell density $c = c_0$. Vorticity and strain can rotate bacterial alignment $\mathbf{p}$ (the flow alignment parameter $\lambda > 1$ for elongated swimmers), with relaxation controlled by the rotational viscosity γ. The last term in equation (1) is the simplest strain-polarization coupling, with τ_R an orientational relaxation time that controls the alignment of bacterial polarization to polymer strain, similar to that in passive liquid crystal elastomers[29]. The DNA is modelled as a standard elastic medium, with Maxwell relaxation time $\tau_p = \eta/G'$ and η the shear viscosity. The flow velocity is determined by the Stokes equation that imposes force balance, $\Gamma(\mathbf{v} - v_0\mathbf{p}) = \nabla(\sigma^{el} + \sigma^a) - \nabla\Pi$, with Γ the substrate friction, v_0 the bacteria swimming speed and Π the pressure required to enforce incompressibility. In the experiments the thickness of the bacterial drop is much smaller than its lateral size, indicating that friction dominates over viscous stresses. The active stress tensor is $\sigma^a = \alpha\mathbf{p}\cdot\mathbf{p}$ (in component form $(\sigma^a)_{ij} = \alpha p_i p_j$) with $\alpha < 0$ for pushers such as *E. coli*. As the active stress is proportional to the average force dipole exerted by the swimmers, we expect $|\alpha| \propto c$. The dynamics is controlled by three competing timescales: the Maxwell relaxation time τ_p, the stress alignment time τ_R, and the active shearing time $\tau_a = \Gamma l_a^2/|\alpha|$, with $l_a \approx \sqrt{K/|c|}$ a characteristic length scale (as in active nematics[30]). Numerical solution of the continuum model (Supplementary Information section III) reproduces the transition from a global vortex state to an oscillatory state with periodic flow reversal (Fig. 2c, d; Supplementary Fig. 2, Supplementary Fig. 3; Supplementary Videos 5, 6) and shows that the transition is controlled by the interplay of these three timescales. An analytical analysis of steady states and their stability (Supplementary Information sections IV and V) confirms the numerics and yields stability boundaries summarized in a phase diagram in Fig. 4b (note that only the high concentration part within by the black box is relevant here). Briefly, increasing τ_p (which grows with DNA concentration) at fixed cell density, the system first transits from the turbulent state to polar laminar flow at $\tau_p = \tau_l \approx \tau_R$ via suppression of the splay instability[1,31], corresponding to a unidirectional giant vortex at a DNA concentration d_1 (~50 ng μl^{-1}) essentially independent of cell density in Fig. 4a, then to an oscillatory state at $\tau_p = \tau_{II} \approx \tau_a \approx K/\alpha^2$ with an oscillation frequency $\omega \approx |\alpha|/\sqrt{\tau_R} \approx 1/\sqrt{\tau_p}$ at threshold, corresponding to an oscillatory giant vortex at a DNA concentration d_2 that decreases with increasing cell density in Fig. 4a. The numerical analysis also suggests that, although in the oscillatory state the bacterial polarization only exhibits small transverse oscillations about its mean direction while the velocity reverses, these transverse polarization fluctuations are responsible for the instability of the giant vortex (see Supplementary Fig. 2). This observation allows us to map the nonlinear dynamics onto the FitzHugh–Nagumo model[32], a well known excitable

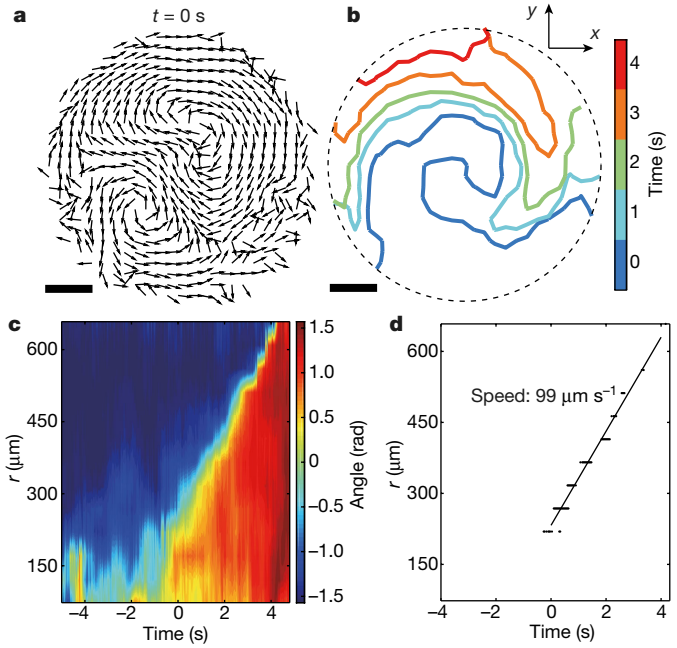

Fig. 3 | Dynamics of chirality switching process in oscillatory giant vortex. **a**, Direction field of collective velocity at the initial stage of a chirality-switching event showing the emergence of a local vortex with opposite chirality (Supplementary Video 3). **b**, Propagation of the 'switching front' (coloured lines; Methods). Colourmap indicates time. Scale bars in **a**, **b**, 250 μm. **c**, Space–time plot (kymograph) of the direction of collective velocities (that is, relative angle between collective velocity and local radial orientation) (Methods). **d**, The propagation speed of the chirality-switching front in **c** is computed by fitting the position of the switching front as a function of time.

relaxation oscillator (Extended Data Fig. 5 and Supplementary Information section VII), and show that the transition to spontaneous oscillations at $\tau_p \approx \tau_a$ is via a Hopf bifurcation, indicating a possible mechanism for the experimental results. Further details of the calculation and simulations can be found in Supplementary Information.

In the experiment, τ_p does indeed approach τ_a when the system transits to oscillations (Extended Data Fig. 6). Consistent with the experimental observations, the transition to oscillations occurs at $\tau_{II} \approx K/\alpha^2$, which decreases with increasing bacterial concentration (activity) (Fig. 4a); and the oscillation frequency ω decreases with addition of DNA (Fig. 4c; Methods), since τ_p increases with DNA concentration (Fig. 4d) and τ_R is expected to behave similarly. This feature is also corroborated by the fully nonlinear simulations (Supplementary Information Fig. 3c–e). On the other hand, ω also increases with activity, hence with bacterial concentration. This is at odds with experiments that find that the oscillation frequency decreases with the concentration of bacteria, but is a generic feature of active-matter models that display relaxation oscillation with[18,28] or without[17,33,34] added polymer. It is unclear at present how this discrepancy may be resolved, but it suggests that the effects of nonlinear viscoelasticity in active fluids deserve more attention.

Despite the success of our theoretical model in explaining the essential phenomena, several open questions remain. First, the model suggests that transverse polarization fluctuations drive the switching of the flow, but more work is needed to firmly establish the connection between the change in sign of the splay ($\nabla \cdot \mathbf{p}$) and flow switching. Second, shear bands are observed in the model (Supplementary Video 5) and only rarely in the experiments. Understanding the role of boundary conditions on shear banding will require extensive simulations of the model. Third, our numerical data are not sufficient to conclusively confirm non-sinusoidal oscillations as shown by experiments (Fig. 2d). Relaxation oscillators in general exhibit sinusoidal (that is, harmonic) oscillations close to the Hopf bifurcation, with the oscillation waveform

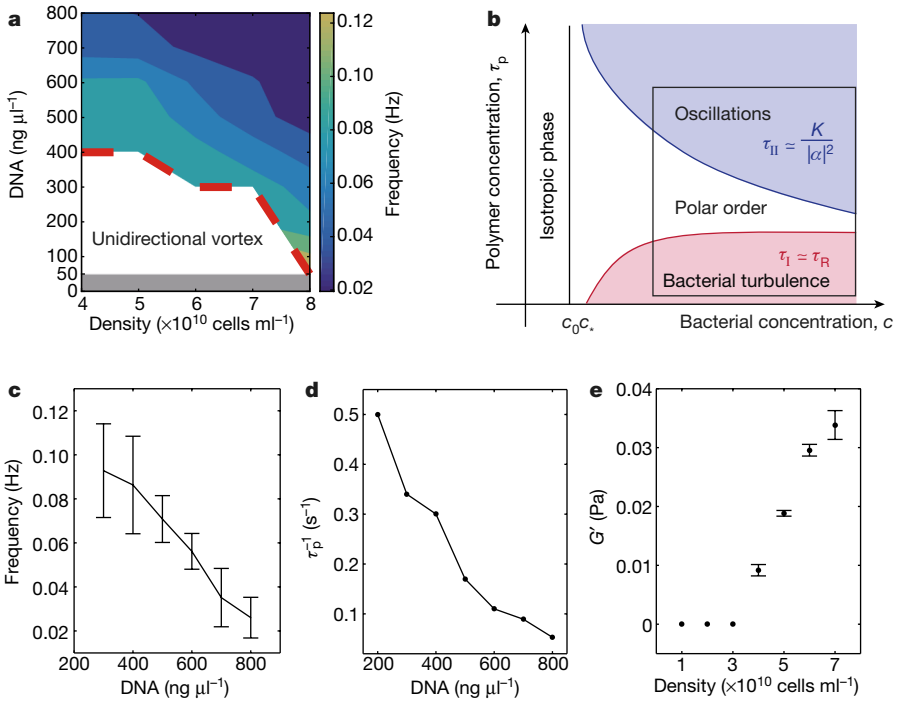

Fig. 4 | Phase diagram of giant vortices and rheology measurement. **a**, Phase diagram from experiments. White area, unidirectional giant vortex; coloured area, oscillatory giant vortex (colourmap indicating chirality-switching frequency); grey area, bacterial turbulence. **b**, Schematic phase diagram from linear instability analysis of the continuum model. We have taken bacterial and DNA concentrations as a proxy for the activity $|\alpha|$ ($\propto c$, with c_* corresponding to the activity threshold for the splay instability) and the Maxwell relaxation time τ_p, respectively. **c**, Chirality-switching frequency in **a** versus DNA concentration at cell density 6×10^{10} cells ml^{-1}. **d**, Inverse of τ_p measured by microrheology as a function of DNA concentration (Methods). **e**, Storage modulus of pure bacterial suspensions versus cell density (Methods; Extended Data Fig. 9). Error bars in **c**, **e** indicate standard variation ($N = 5$ and $N = 10$, respectively).

becoming strongly anharmonic far from threshold. Hence the approximate sinusoidal nature of the oscillations in the simulation may be a result of proximity to the Hopf bifurcation. Finally, the numerical resolution is too low to resolve the switching dynamics of giant vortices. In the experiments, there may be other timescales that slow down the switching dynamics. Addressing this will require augmenting the model and is left for future work.

Our model suggests that the ultra-long relaxation times (τ_p) of high molecular weight DNA[25] are key to the spatial-temporal order that we revealed. Indeed, we have observed the formation of giant vortices with other types of high-molecular-weight DNA with τ_p of the order of seconds, but not with viscoelastic polymers with τ_p at the millisecond scale (Methods; Extended Data Fig. 7). On the other hand, increasing medium viscosity tends to reduce cell speed and does not promote the formation of giant vortices (Extended Data Fig. 8). Also, the storage modulus (G') of the polymer must be large enough that the resulting elastic stress can affect the collective motion pattern of the bacteria[35]. DNA viscoelasticity contributes to G', but we found that bacterial suspensions without additive polymers also display elasticity (~0.01 Pa) above cell density of about 4×10^{10} cells ml^{-1} (Fig. 4e; measured on the scale of ~100 μm), which coincides with the critical cell density required for the onset of unidirectional giant vortex. In addition, we stress that spatial confinement is essential, as we could not observe the giant vortex in bacterial suspension drops with a diameter above ~3.3 mm. Nonetheless, by varying the size of suspension drops from ~1 mm to ~2.5 mm, we found that the threshold for the transition from bacterial turbulence to the giant vortex (d_1) is largely insensitive to confinement size (Methods; Extended Data Fig. 10).

Taken together, our results demonstrate that tuning fluid viscoelasticity provides a simple means for manipulating the self-organization of bacterial active matter in space and time. Bacteria in biofilms and animal gastrointestinal tracts often swim in viscoelastic fluids abundant in long-chain polymers, including extracellular DNA[36]. Our findings suggest that, above a threshold bacterial density, the viscoelasticity of the environment may modify the collective motion patterns of bacteria, thereby influencing the dispersal of biofilms and the translocation of gut microbiome.

We have developed a minimal active-matter model that explains our findings as arising from the interplay between polymer viscoelastic relaxation and the rate of active forcing. Our work may shed light on the role of environment viscoelasticity in other active systems, such as cytoskeletal fluids[9,10] and active gels[11]. It may also pave the way to the development of a new class of adaptive self-driven devices and materials that exploits the feedback between activity and viscoelasticity.

Online content

Any methods, additional references, Nature Research reporting summaries, source data, extended data, supplementary information, acknowledgements, peer review information; details of author contributions and competing interests; and statements of data and code availability are available at https://doi.org/10.1038/s41586-020-03168-6.

1. Marchetti, M. C. et al. Hydrodynamics of soft active matter. *Rev. Mod. Phys.* **85**, 1143–1189 (2013).
2. Danino, T., Mondragon-Palomino, O., Tsimring, L. & Hasty, J. A synchronized quorum of genetic clocks. *Nature* **463**, 326–330 (2010).
3. Sokolov, A. & Aranson, I. S. Physical properties of collective motion in suspensions of bacteria. *Phys. Rev. Lett.* **109**, 248109 (2012).
4. Wensink, H. H. et al. Meso-scale turbulence in living fluids. *Proc. Natl Acad. Sci. USA* **109**, 14308–14313 (2012).
5. Chen, C., Liu, S., Shi, X. Q., Chaté, H. & Wu, Y. Weak synchronization and large-scale collective oscillation in dense bacterial suspensions. *Nature* **542**, 210–214 (2017).
6. Saw, T. B. et al. Topological defects in epithelia govern cell death and extrusion. *Nature* **544**, 212–216 (2017).
7. Kawaguchi, K., Kageyama, R. & Sano, M. Topological defects control collective dynamics in neural progenitor cell cultures. *Nature* **545**, 327–331 (2017).
8. Keber, F. C. et al. Topology and dynamics of active nematic vesicles. *Science* **345**, 1135–1139 (2014).
9. Wu, K.-T. et al. Transition from turbulent to coherent flows in confined three-dimensional active fluids. *Science* **355**, eaal1979 (2017).
10. Huber, L., Suzuki, R., Krüger, T., Frey, E. & Bausch, A. R. Emergence of coexisting ordered states in active matter systems. *Science* **361**, 255–258 (2018).
11. Prost, J., Jülicher, F. & Joanny, J. F. Active gel physics. *Nat. Phys.* **11**, 111–117 (2015).
12. Palacci, J., Sacanna, S., Steinberg, A. P., Pine, D. J. & Chaikin, P. M. Living crystals of light-activated colloidal surfers. *Science* **339**, 936–940 (2013).
13. Bricard, A., Caussin, J.-B., Desreumaux, N., Dauchot, O. & Bartolo, D. Emergence of macroscopic directed motion in populations of motile colloids. *Nature* **503**, 95–98 (2013).
14. Yan, J. et al. Reconfiguring active particles by electrostatic imbalance. *Nat. Mater.* **15**, 1095–1099 (2016).
15. Karig, D. et al. Stochastic Turing patterns in a synthetic bacterial population. *Proc. Natl Acad. Sci. USA* **115**, 6572–6577 (2018).
16. Vicker, M. G. Eukaryotic cell locomotion depends on the propagation of self-organized reaction–diffusion waves and oscillations of actin filament assembly. *Exp. Cell Res.* **275**, 54–66 (2002).
17. Giomi, L., Mahadevan, L., Chakraborty, B. & Hagan, M. F. Banding, excitability and chaos in active nematic suspensions. *Nonlinearity* **25**, 2245 (2012).
18. Hemingway, E. J. et al. Active viscoelastic matter: from bacterial drag reduction to turbulent solids. *Phys. Rev. Lett.* **114**, 098302 (2015).
19. Wehner, M. et al. An integrated design and fabrication strategy for entirely soft, autonomous robots. *Nature* **536**, 451–455 (2016).
20. Preston, D. J. et al. Digital logic for soft devices. *Proc. Natl Acad. Sci. USA* **116**, 7750–7759 (2019).
21. Wioland, H., Woodhouse, F. G., Dunkel, J., Kessler, J. O. & Goldstein, R. E. Confinement stabilizes a bacterial suspension into a spiral vortex. *Phys. Rev. Lett.* **110**, 268102 (2013).
22. López, H. M., Gachelin, J., Douarche, C., Auradou, H. & Clément, E. Turning bacteria suspensions into superfluids. *Phys. Rev. Lett.* **115**, 028301 (2015).
23. Bozorgi, Y. & Underhill, P. T. Effects of elasticity on the nonlinear collective dynamics of self-propelled particles. *J. Non-Newton. Fluid Mech.* **214**, 69–77 (2014).
24. Li, G. & Ardekani, A. M. Collective motion of microorganisms in a viscoelastic fluid. *Phys. Rev. Lett.* **117**, 118001 (2016).
25. Liu, Y., Jun, Y. & Steinberg, V. Concentration dependence of the longest relaxation times of dilute and semi-dilute polymer solutions. *J. Rheol.* **53**, 1069–1085 (2009).
26. Ginoux, J. M. & Letellier, C. Van der Pol and the history of relaxation oscillations: toward the emergence of a concept. *Chaos* **22**, 023120 (2012).
27. Sokolov, A., Aranson, I. S., Kessler, J. O. & Goldstein, R. E. Concentration dependence of the collective dynamics of swimming bacteria. *Phys. Rev. Lett.* **98**, 158102 (2007).
28. Hemingway, E. J., Cates, M. E. & Fielding, S. M. Viscoelastic and elastomeric active matter: linear instability and nonlinear dynamics. *Phys. Rev. E* **93**, 032702 (2016).
29. Warner, M. & Terentjev, E. M. *Liquid Crystal Elastomers* (Oxford Univ. Press, 2007).
30. Doostmohammadi, A., Ignés-Mullol, J., Yeomans, J. M. & Sagués, F. Active nematics. *Nat. Commun.* **9**, 3246 (2018).
31. Aditi Simha, R. & Ramaswamy, S. Hydrodynamic fluctuations and instabilities in ordered suspensions of self-propelled particles. *Phys. Rev. Lett.* **89**, 058101 (2002).
32. Murray, J. D. *Mathematical Biology: I. An Introduction* (Springer, 2007).
33. Giomi, L., Mahadevan, L., Chakraborty, B. & Hagan, M. F. Excitable patterns in active nematics. *Phys. Rev. Lett.* **106**, 218101 (2011).
34. Woodhouse, F. G. & Goldstein, R. E. Spontaneous circulation of confined active suspensions. *Phys. Rev. Lett.* **109**, 168105 (2012).
35. Benzi, R. & Ching, E. S. C. Polymers in fluid flows. *Annu. Rev. Condens. Matter Phys.* **9**, 163–181 (2018).
36. Whitchurch, C. B., Tolker-Nielsen, T., Ragas, P. C. & Mattick, J. S. Extracellular DNA required for bacterial biofilm formation. *Science* **295**, 1487 (2002).

Publisher's note Springer Nature remains neutral with regard to jurisdictional claims in published maps and institutional affiliations.

© The Author(s), under exclusive licence to Springer Nature Limited 2021

Methods

No statistical methods were used to predetermine sample size.

Bacterial strains

Two *E. coli* strains were used: HCB1737 (a derivative of *E. coli* AW405; from H. Berg, Harvard University) and HCB1737 GFP (HCB1737 with constitutive expression of green fluorescent protein encoded on the plasmid pAM06-tet[37]; from A. Mukherjee and C. M. Schroeder, University of Illinois at Urbana-Champaign). Single-colony isolates were grown overnight (~13–14 h) with shaking (180 r.p.m.) in LB medium (1% Bacto-tryptone, 0.5% yeast extract, 0.5% NaCl) at 30 °C to stationary phase. For HCB1737 GFP, kanamycin (50 μg ml^{-1}) was added to the growth medium to maintain the plasmid. For single-cell tracking, HCB1737 GFP was mixed with HCB1737 at a ratio of 1:20,000.

DNA purification

E. coli genome DNA was purified with Genomic DNA Purification Kit (Promega catalogue no. A1120), following the manufacturer's protocol. Briefly, overnight culture of *E. coli* was centrifuged and upon removal of the supernatant, Nuclei Lysis Solution (Promega) was added to resuspend the pellet. Then the suspension was supplemented with RNase Solution (Promega) and incubated. After incubation, the suspension was supplemented with Protein Precipitation Solution (Promega), vortexed and centrifuged to obtain the supernatant. The supernatant was transferred to a tube containing isopropanol at room temperature. The tube was gently and repeatedly inverted until thread-like DNA appeared. Aqueous DNA solutions were obtained by centrifugation (to remove isopropanol) followed by rehydration in DNA Rehydration Solution (Promega). To prepare DNA solutions to be supplemented in bacterial suspensions, the DNA Rehydration Solution (Promega) was replaced by LB medium. DNA concentration was measured by spectrophotometer (NanoDrop, Thermo Fisher).

Agar plate and bacterial suspension drop

LB agar (0.6% Difco Bacto-agar infused with LB medium) was autoclaved and stored at room temperature. Before use, the agar was melted in a microwave oven, cooled to ~60 °C and pipetted in 10-ml aliquots into 90-mm polystyrene Petri plates. The plates were swirled gently to ensure surface flatness, and then cooled for 10 min without a lid inside a large Plexiglas box. Overnight bacterial cultures were treated with DNase I (200 units ml^{-1}; Thermo Fisher catalogue number 18047019) for ~5 min, washed by centrifugation (7,000*g*, 3 min), and resuspended to desired cell densities. The cell suspension was then supplemented with purified *E. coli* genomic DNA at desired concentrations and deposited onto LB agar surface at appropriate volume (a liquid drop with diameter ~1.5 mm requires ~0.03 μl bacterial suspension).

Imaging cells

Collective motion of bacterial suspension was observed in phase contrast with a 4× objective (Nikon Plan Fluor 4×, numerical aperture 0.13, working distance 16.5 mm) mounted on an inverted microscope (Nikon Eclipse Ti). Recordings were made with an sCMOS camera (Andor Zyla 4.2) at 30 frames per second (f.p.s.). For single-cell tracking, HCB1737 GFP cells were imaged in epifluorescence with a 20× objective (Nikon S Plan Fluor 20×, numerical aperture 0.45, working distance 8.2–6.9 mm) and an FITC filter cube (excitation 482/35 nm, emission 536/40 nm, dichroic 506 nm; ITC-3540C-000, Semrock Inc.), with the excitation light provided by a mercury precentred fibre illuminator (Nikon Intensilight); meanwhile, the background bacterial collective motion was imaged in phase contrast through the same optical system, with the illumination light provided by a white-light LED (Thorlabs catalogue number MCWHL5). The camera was configured to record at 40 f.p.s.; fluorescent and phase-contrast images were recorded in alternate frames at 20 f.p.s. The camera was controlled by NIS Elements (Nikon); the white-light LED was switched on only during the acquisition of phase-contrast images and was triggered by 20 Hz transistor–transistor logic (TTL) signals sent from a custom-programmed Arduino microcontroller that modulated the 40-Hz fire output from the camera. In all experiments, the Petri dishes were covered with a lid to prevent evaporation and air convection, and the sample temperature was maintained at 30 °C by a custom-built temperature control system installed on the microscope stage.

Analysis of collective velocity field in giant vortex

The velocity field of bacterial collective motion $\mathbf{v}(\mathbf{r}, t)$ was obtained by performing PIV on phase-contrast microscopy images with an open-source package MatPIV 1.6.1 written by J. Kristian Sveen (http://folk.uio.no/jks/ matpiv/index2.html). For each pair of consecutive images obtained with the 4× objective, the PIV interrogation-window size started at 104 μm × 104 μm and ended at 26 μm × 26 μm after three iterations. The grid size of the resulting velocity field was 13 μm × 13 μm. To visualize the collective velocity field obtained by PIV analysis, the velocity field was coarse-grained and plotted on a square mesh with grid spacing of 60 μm or 100 μm. The direction of collective velocity is defined as $\hat{\mathbf{v}}(\mathbf{r}, t) = \mathbf{v}(\mathbf{r}, t)/|\mathbf{v}(\mathbf{r}, t)|$. The vortex order parameter, that is, mean vortical flow $\langle V_\theta \rangle$, or normalized mean vortical flow (P), is defined as $\langle V_\theta \rangle = \langle \mathbf{v}(\mathbf{r}, t) \cdot \mathbf{e}_\theta \rangle_{r,\theta}$ or $P(t) = \langle \mathbf{v}(\mathbf{r}, t) \cdot \mathbf{e}_\theta / |\mathbf{v}(\mathbf{r}, t)| \rangle_{r,\theta}$, respectively, where $\mathbf{e}_\theta$ is the unit vector along the tangential direction (in the polar coordinate system whose origin is located at the centre of the suspension drop) and the angular brackets indicate averaging over polar coordinates r and θ. P being equal to +1 (or −1) indicates a perfectly ordered CCW (or CW) vortex. Unidirectional giant vortexes typically have $|P| > 0.6$ averaged over time. The chirality of the unidirectional giant vortex is slightly more CCW than CW (30:24).

Analysis of single-cell motion in giant vortex

Single cells were tracked for at least 10 s in fluorescent images using the MTrackJ plugin developed for ImageJ. The duration of cell trajectories shown in Fig. 1e and Extended Data Fig. 2b was ~25 s. The background bacterial collective velocity field was computed by performing PIV analysis on phase-contrast images obtained simultaneously with the fluorescent images; the PIV interrogation-window size started at 41.6 μm × 41.6 μm and ended at 10.4 μm × 10.4 μm after three iterations, with the grid size of the resulting velocity field being 5.2 μm × 5.2 μm. To compute the drift-corrected MSD of single cells (Fig. 1e; Extended Data Fig. 2c), the local advective drift was taken as the average of bacterial collective velocity in a circular region with a radius of 15 μm and centred at the tracked bacterium, and then the obtained local advective drift was subtracted from the velocity of the cell. The resulted drift-corrected single-cell velocity was integrated over time to find the drift-corrected displacement, which was further used to calculate the MSD. In other words, the drift-subtracted MSD represents fluctuations of single-cell velocity with respect to the advective drift of the giant vortex. The local diffusion constant D in Fig. 1e obtained by fitting the MSD at $t > 2$ s to $4Dt$ was 317 μm^2 s^{-1}. In the laboratory frame, MSD of single cells was computed without subtracting the advective drift and was fitted to $4Dt^\alpha$ to yield the exponent α. According to the result shown in Extended Data Fig. 2a, individual cells in a unidirectional giant vortex analysed in Fig. 1e underwent ballistic motion in the laboratory frame ($\alpha \approx 1.8$) at short timescales (less than ~0.4 s). At intermediate timescales (2.4 s < t < 3.5 s), the motion was dominated by diffusive behaviour ($\alpha \approx 1.1$). At longer timescales (4 s < t < 20 s), the influence of the advective drift became dominant ($\alpha \approx 1.3$), since the Péclet number (Pe) of bacterial transport was $\mathrm{Pe} = Lu/D \approx 30 \gg 1$, where L is the vortex size (~1,000 μm), u is the typical drift speed (~10 μm s^{-1}) and $D \approx 300$ μm^2 s^{-1}.

Definition and computation of chirality-switching front

During chirality switching, a local vortex with opposite chirality tended to emerge near the periphery of the giant vortex, grew and eventually

took over the entire system. The whole process typically lasted less than 10 s. During chirality switching process, the direction of collective velocity vectors at the boundary between the original giant vortex and the newly emerged vortex with opposite chirality flipped by ~180° rapidly (within ~1 s) in a non-coordinated manner (that is, some vectors rotated CW and some CCW). Meanwhile, the relative angle between collective velocity vectors and local radial orientation, which is defined as $\beta = (\pi/2) - \cos^{-1}(\mathbf{v}(\mathbf{r}, t) \cdot \mathbf{e}_\theta / |\mathbf{v}(\mathbf{r}, t)|)$, changed from about $-\pi/2$ to about $+\pi/2$ (CW to CCW) or about $+\pi/2$ to about $-\pi/2$ (CCW to CW). This allowed us to define the chirality switching front at any given instant as the contour line of zero relative angle between collective velocity and local radial orientation, that is, the locus of positions where the collective velocity points radially either towards or away from the drop centre. For the space–time plot (kymograph) of the direction of collective velocities (Fig. 3c), the region of analysis was chosen along the $2\pi/3$ direction with respect to the $+x$ axis in the coordinate system of Fig. 3b.

Transition from bacterial turbulence to unidirectional giant vortex

To compute the DNA concentration threshold (d_1) for the transition from bacterial turbulence to unidirectional giant vortex, the vortex order (that is, normalized mean vortical flow P) as a function of DNA concentration was fitted to a modified sigmoid function $P(x) = \frac{a_3}{1+\exp[-a_1(x-a_2)]} + a_4$, where x represents the DNA concentration, $P(x)$ represents vortex order, and a_1, a_2, a_3, a_4 are fitting parameters. The threshold DNA concentration d_1 was computed by defining the giant vortex state as having mean vortex order >0.6 (that is, by solving $P(x) = 0.6$), and the uncertainty of d_1 was computed based on the fitting error of parameters. For the case with *E. coli* genomic DNA (Extended Data Fig. 3), due to large variation of normalized mean vortical flow among suspension drops with identical compositions below DNA concentration 50 ng μl^{-1}, the computed threshold d_1 has large uncertainty (30 ± 18 ng μl^{-1}). So we take d_1 for *E. coli* genomic DNA to be approximately 50 ng μl^{-1} when plotting the phase diagram in Fig. 4a.

Rheology of bacterial suspension

Rheological measurements of bacteria suspension were performed in a rheometer (Anton Paar Physica MCR 301). The plate used for oscillatory shear measurements was CP50-1 (diameter 49.972 mm, angle 0.990° and 99 μm gap; Anton Paar, part no. 79040 serial 20173). The storage modulus (G_e) and loss modulus as a function of frequency were measured in frequency sweep mode (constant strain amplitude) by imposing 10% maximal strain. For each sample, 25 measurements were made at any given frequency and the results were averaged. A solvent trap equipped in the rheometer was used to reduce evaporation. Before rheology measurement, bacterial overnight cultures were treated with DNase I (80 units ml^{-1}) for ~5 min, washed by motility buffer (0.01 M potassium phosphate, 0.067 M NaCl, 10^{-4} M EDTA, pH 7.0) and concentrated by centrifugation at 5,000*g*, 4 min, to desired densities.

Microrheology of DNA solution

Bulk-rheology measurement described above does not have sufficient resolution to probe the low-frequency viscoelasticity of DNA solutions, so we switched to microrehology measurement (Extended Data Fig. 9b)[38,39]. DNA solutions (in DNA Rehydration Solution; Promega) were supplemented with 0.5-μm-diameter microspheres (Thermo Fisher, cat. no: F8812) and sealed by Vaseline in glass chamber with depth ~200 μm. MSD of microspheres were measured by tracking the microspheres in DNA solution based on phase-contrast images taken with a 60× air objective (Nikon Plan Apo λ, numerical aperture 0.95, working distance 0.20–0.11 mm) and a 1.5× relay lens equipped on the microscope. The focal plane was chosen at the middle of glass chamber. For each sample, around six different beads were recorded with the sCMOS camera (Andor Zyla 4.2) at 25 f.p.s. each for a duration of ~5–10 min. Measurements were made at room temperature to prevent advection caused by temperature inhomogeneity. The particle trajectories were analysed with a custom-written programme in MATLAB (The MathWorks; Natick). Dynamic modulus of DNA solutions was computed based on the MSD of microspheres and a frequency-dependent Stokes–Einstein equation[38], using an algorithm implemented in MATLAB (Kilfoil Lab in University of Massachusetts Amherst). Note that this microrheology measurement was not suitable for DNA solutions lower than 200 ng μl^{-1}, as microspheres stayed in the focal plane for shorter durations, and consequently the MSD calculation was less accurate. The longest relaxation time of DNA in solutions (τ_p) was calculated in two ways[40]. (1) τ_p can be obtained from the lowest crossover frequency (denoted as ω_c) between storage modulus (G') and loss modulus (G'') as $\tau_p = 1/\omega_c$. (2) For DNA solutions without lowest crossover frequency, τ_p was computed from $\tau_p = 12(\eta - \eta_s)/(\pi^2 G)$, where η is the low shear viscosity obtained by fitting the low-frequency loss modulus as $G'' = \eta\omega$, η_s is the viscosity of buffer and G is the high-frequency plateau value of the storage modulus G'.

Dependence of giant vortex state on polymer molecular weight

In addition to *E. coli* genomic DNA, lambda phage DNA (~48,500 bp, molecular weight ~3.15×10^7 Da; Sigma, catalogue number D9768) and salmon testes DNA (~2,000 bp, molecular weight 1.3×10^6 Da; Sigma, catalogue number D1626) were used. As shown in Extended Data Fig. 7, the DNA concentration threshold (d_1) for the transition from bacterial turbulence to unidirectional giant vortex decreases with increasing molecular weight of DNA polymers. The dependence of the threshold concentration d_1 seems to be consistent with the power-law scaling predicted for the effect of a dilute polymer solution on flow alignment and nematic viscosity[41]. We did not observe the formation of giant vortices with either methyl cellulose (molecular weight ~86 kDa; Sigma-Aldrich catalogue number H7509) or poly vinylpropylene (PVP, molecular weight ~360 kDa; Sigma-Aldrich catalogue number 81440), whose relaxation times are at the millisecond scale. On the other hand, the chances of developing an oscillatory giant vortex were low in bacterial suspension drops supplemented with lambda phage DNA and salmon testes DNA. In the concentration range of salmon testes DNA we tested, we did not observe any oscillatory giant vortex. For lambda phage DNA, we observed an oscillatory giant vortex in one suspension drop among a total of ~30 recorded at DNA concentration 500 ng μl^{-1}, and in two out of ~40 at DNA concentration 800 ng μl^{-1}. The reason could be due to the relatively small Maxwell relaxation time yet high viscosity of these DNA solutions compared with *E. coli* genomic DNA solutions at the same concentration. Indeed, as determined by microrheology measurement (see above), the relaxation time for salmon testes DNA solution at concentration as high as 4,000 ng μl^{-1} was ~0.9 s, which is smaller than the relaxation time of *E. coli* genomic DNA solution at 200 ng μl^{-1} (~2.0 s). The relaxation time for lambda phage DNA solution at concentration 800 ng μl^{-1} was ~4.2 s, but its viscosity is substantially higher than 400 ng μl^{-1} *E. coli* genomic DNA solution with a comparable relaxation time (~3 s). In the instability analysis, the unidirectional vortex transits to an oscillatory vortex when the polymer relaxation time τ_p grows larger than $\tau_{II} = 2\Gamma l/[a^2(\lambda - 1)(|\alpha| - \alpha_c^s)]$ (see equation (28) in Supplementary Information; here α_c^s is the activity threshold for the splay instability). In this expression, τ_{II} depends on the friction between the fluid and the substrate Γ, and Γ is proportional to the total viscosity of the fluid. Hence the τ_{II} for bacterial suspensions with 800 ng μl^{-1} lambda phage DNA is expected to be higher than that for bacterial suspensions with 400 ng μl^{-1} *E. coli* genomic DNA. Consequently, the probability of having oscillations in bacterial suspensions with 800 ng μl^{-1} lambda phage DNA would be lower, even though the relaxation times τ_p are similar.

Confinement effect on the development of giant vortex state

Bacterial suspension drops do not form giant vortices without confinement. Without spatial confinement (for example, in centimetre-scale bacterial swarming colonies), dense bacterial active fluids can display collective oscillatory motion as reported previously[5]. There is a distinct difference between the collective oscillatory motion and the oscillatory

giant vortex described in this paper. The collective oscillatory motion arises from diffusive coupling of random trajectories, rather than from viscoelastic stresses; its emergence does not require additive DNA, and the oscillation frequency is independent of cell density as shown in Extended Data Fig. 10a. In addition, collective oscillatory motion does not form a vortex: the collective velocity field is uniform both in direction and magnitude over several millimetres at any instant. By varying the size of suspension drops from ~1 mm to ~2.5 mm, we found that in oscillatory giant vortices both the oscillation frequency and vortical flow amplitude appeared independent of confinement size (Extended Data Fig. 10b, c). In addition, the DNA concentration threshold for the transition from bacterial turbulence to unidirectional giant vortex was largely insensitive to confinement size (Extended Data Fig. 10d–f). Taken together, spatial confinement is necessary but not sufficient for giant vortex development.

Data availability

The data supporting the findings of this study are included within the paper and its Supplementary Materials.

Code availability

The custom codes used in this study are available from the corresponding author upon request.

37. Mukherjee, A., Walker, J., Weyant, K. B. & Schroeder, C. M. Characterization of flavin-based fluorescent proteins: an emerging class of fluorescent reporters. *PLoS ONE* **8**, e64753 (2013).
38. Mason, T. G., Ganesan, K., van Zanten, J. H., Wirtz, D. & Kuo, S. C. Particle tracking microrheology of complex fluids. *Phys. Rev. Lett.* **79**, 3282–3285 (1997).
39. Zhu, X., Kundukad, B. & van der Maarel, J. R. Viscoelasticity of entangled λ-phage DNA solutions. *J. Chem. Phys.* **129**, 185103 (2008).
40. Kundukad, B. & van der Maarel, J. R. C. Control of the flow properties of DNA by topoisomerase II and its targeting inhibitor. *Biophys. J.* **99**, 1906–1915 (2010).
41. Brochard, F. Viscosities of dilute polymer solutions in nematic liquids. *J. Polym. Sci. Polym. Phys. Ed.* **17**, 1367–1374 (1979).

Acknowledgements We thank Y. Li and W. Zuo for building the image acquisition and microscope stage temperature control systems, H. C. Berg (Harvard University) for providing the bacterial strains, A. Mukherjee and C. M. Schroeder (UIUC) for providing the pAM06-tet plasmid, and L. Xu (CUHK) for assistance with bulk rheology measurement. We thank E. S.C. Ching (CUHK), K. Xia (CUHK) and T. Ngai (CUHK) for discussions and comments. This work was supported by the National Natural Science Foundation of China (NSFC no. 31971182, to Y.W.), the Research Grants Council of Hong Kong SAR (RGC Ref. No. 14303918 and CUHK Direct Grants; to Y.W.), the US National Science Foundation Grant DMR-1609208 (to M.C.M and S.S) and KITP under grant no. PHY-1748958. S.S. is supported by the Harvard Society of Fellows. M.C.M and S.S thank the KITP for hospitality in the course of this work.

Author contributions S.L. discovered the phenomena, designed the study, performed experiments, and analysed and interpreted the data. S.S. and M.C.M. developed the active-matter model, and analysed and interpreted the data. Y.W. conceived the project, designed the study, and analysed and interpreted the data. Y.W. wrote the first draft. All authors contributed to the revision of the paper.

Competing interests The authors declare no competing interests.

Additional information
Supplementary information The online version contains supplementary material available at https://doi.org/10.1038/s41586-020-03168-6.
Correspondence and requests for materials should be addressed to Y.W.
Peer review information *Nature* thanks the anonymous reviewer(s) for their contribution to the peer review of this work.
Reprints and permissions information is available at http://www.nature.com/reprints.

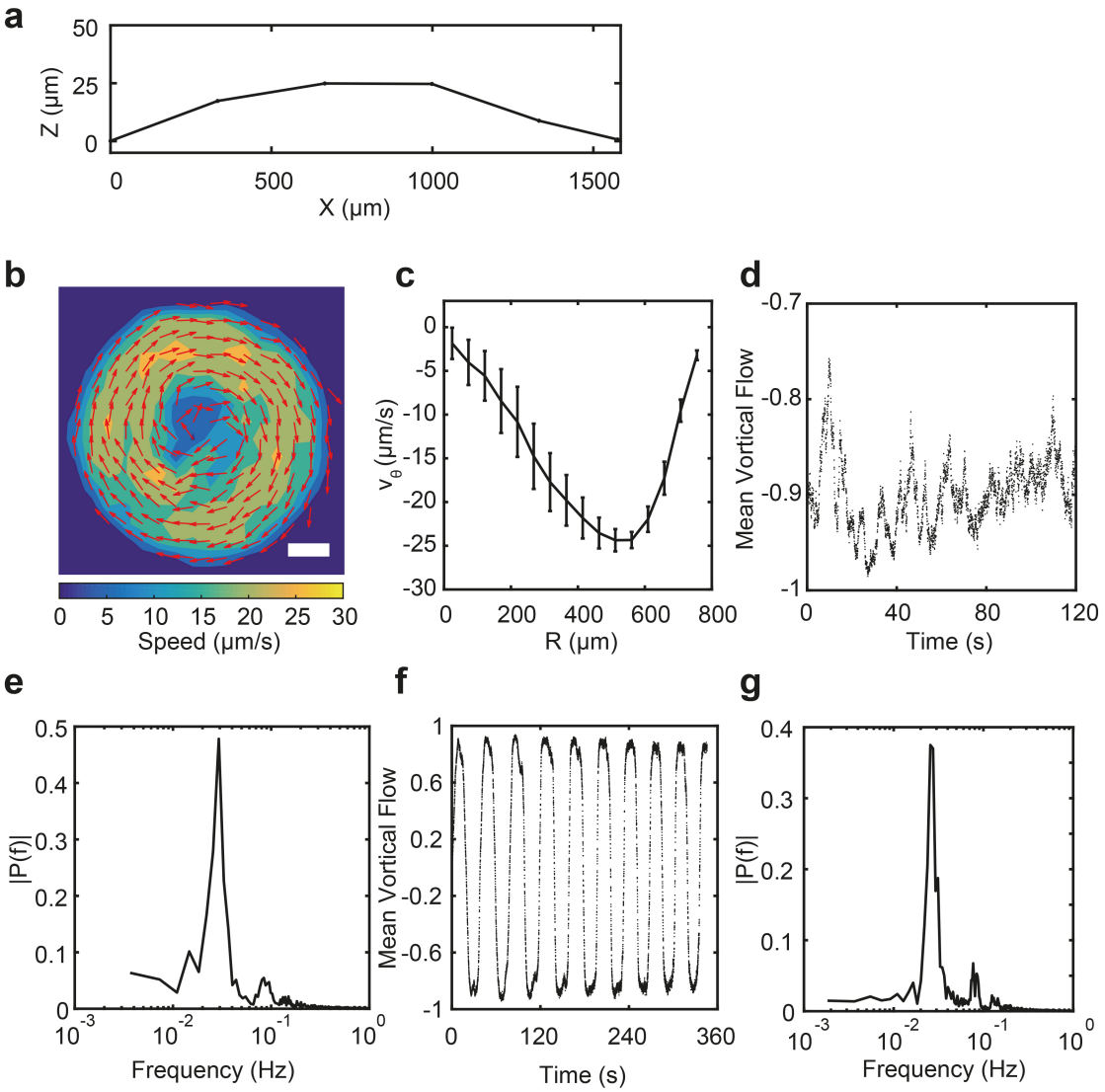

Extended Data Fig. 1 | Height profile of bacterial suspension drop and further characterization of giant vortices. a, Height profile of a bacterial suspension drop measured by locating the uppermost and the lowermost focal planes where fluorescently labelled cells could be found. **b**, Instantaneous velocity field of a representative CW unidirectional giant vortex. Arrows and colourmap represent collective velocity direction and magnitude, respectively (Methods). Cell density, 6×10^{10} cells ml^{-1}; DNA concentration, 200 ng μl^{-1}. Scale bar, 250 μm. **c**, Time- and azimuthally averaged tangential velocity v_θ of the CW giant vortex in **b** plotted against radial position. Error bars represent standard deviation (N = 1,000 successive frames). **d**, Normalized mean vortical flow of the CV giant vortex in **b** (Methods). **e**–**g**, Fourier analysis of the normalized mean vortical flow ($P(t)$) in oscillatory giant vortices. **e**, Fourier spectrum $|P(f)|$ for $P(t)$ in Fig. 2b computed by fast Fourier transform, peaking at ~0.030 Hz and with a full-width at half-maximum (FWHM) of ~0.012 Hz. **f**, $P(t)$ of an oscillatory vortex with nine periods (cell density, ~6×10 cells ml^{-1}; DNA concentration, ~800 ng μl^{-1}). **g**, Fourier spectrum $|P(f)|$ for $P(t)$ in panel **f**, peaking at ~0.026 Hz and with a FWHM of ~0.008 Hz.

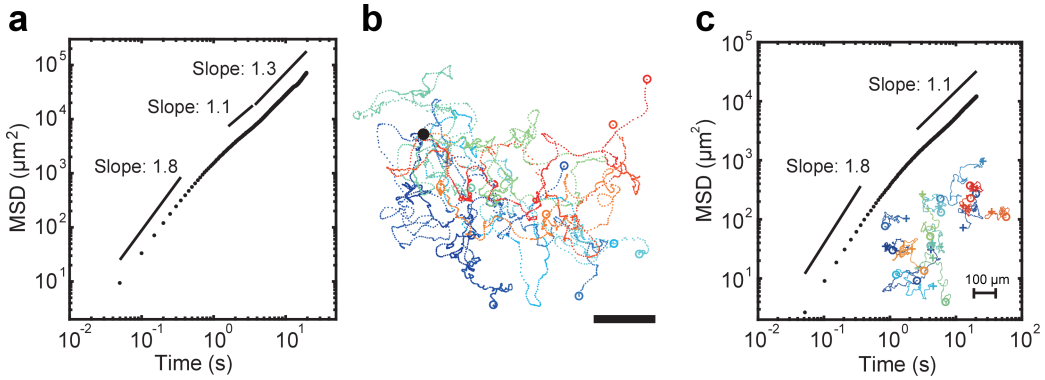

Extended Data Fig. 2 | Diffusive behaviour of single cells in giant vortices. **a**, The mean square displacement (MSD) of individual cells analysed in Fig. 1e in the laboratory frame (Methods). See more discussion in Methods. **b**, Bacterial trajectories in Fig. 1e replotted with the starting points shifted to the same position (black dot). Different colour indicates different bacterium. Scale bar, 100 μm. **c**, Local diffusive behaviour of individual bacteria in an oscillatory giant vortex. MSD of cells was computed based on drift-subtracted single-cell trajectories. In a frame comoving with the giant vortex, individual cells underwent ballistic motion at short timescale (~1 s) and diffusive motion over longer timescales. The diffusion constant D was obtained by fitting the MSD at $t > 2$ s to $4Dt^{\alpha}$, yielding $D \approx 110\ \mu m^2\ s^{-1}$ and $\alpha \approx 1.1$. In this oscillatory giant vortex, DNA concentration was ~500 ng μl^{-1} and cell density was ~6×10^{10} cells ml^{-1}. Inset: trajectories of 14 representative cells (+, starting point; ○, ending point). The time duration of each trajectory is ~28 s, about one period of the oscillatory giant vortex.

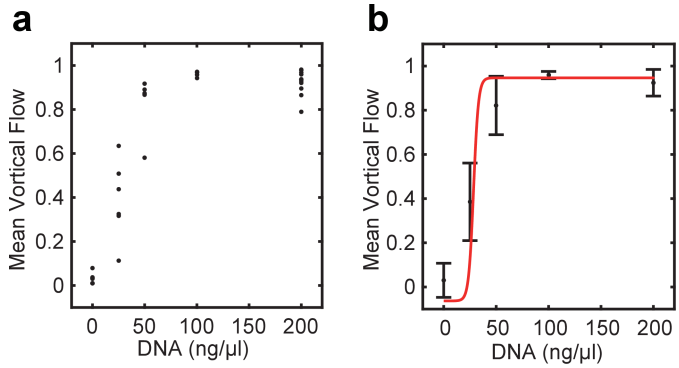

Extended Data Fig. 3 | Vortex order of bacterial suspension drop versus *E. coli* DNA concentration. The diameters of suspension drops were ~1.5 mm. Cell density was fixed at 6×10 cells ml^{-1}. **a**, Scattered data points of vortex order (that is, normalized mean vortical flow P) versus DNA concentration. Each data point represents the normalized mean vortical flow averaged over a time window of ~20 s for one suspension drop with specific DNA concentration. **b**, Sigmoidal fit of P as a function of DNA concentration. The mean and standard deviation (error bars, $N \geq 4$) plotted in **b** were computed based on the scattered data points in **a**. The data in **b** was fitted to a modified sigmoid function (Methods). See more discussion in Methods.

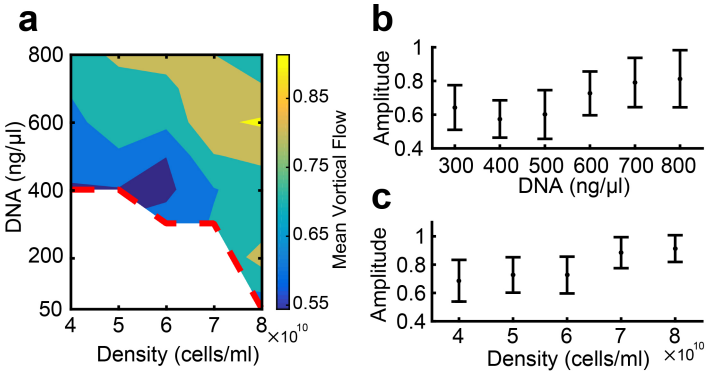

Extended Data Fig. 4 | Dependence of mean-vortical-flow amplitude of oscillatory giant vortices on cell density and DNA concentration. The mean-vortical-flow amplitude of a specific oscillatory giant vortex is taken as the averaged absolute value of extremums of the normalized mean vortical flow. **a**, Contour plot of mean-vortical-flow amplitude (indicated by the colourmap) in the plane of cell density and DNA concentration. Each data point in the contour plot is the average of mean-vortical-flow amplitude from at least three oscillatory giant vortices with the corresponding DNA concentration and cell density. **b**, The mean-vortical-flow amplitude in panel **a** plotted against DNA concentration at fixed cell density ~6×10 cells ml^{-1}. **c**, Mean-vortical-flow amplitude in **a** plotted against cell density at fixed DNA concentration ~600 ng μl^{-1}. Error bars in **b**, **c** indicate standard deviation ($N \geq 3$). Overall, the mean-vortical-flow amplitude of oscillatory giant vortices increases weakly with increasing DNA concentration and cell density.

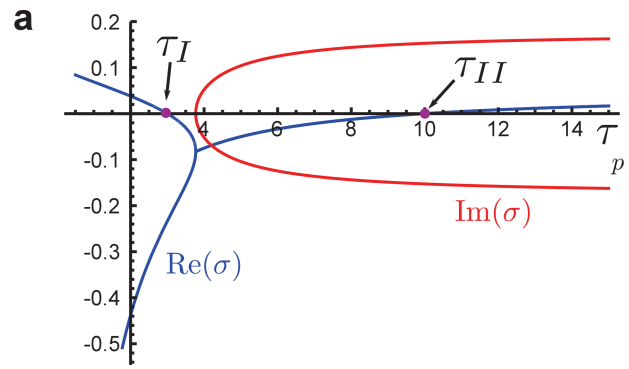

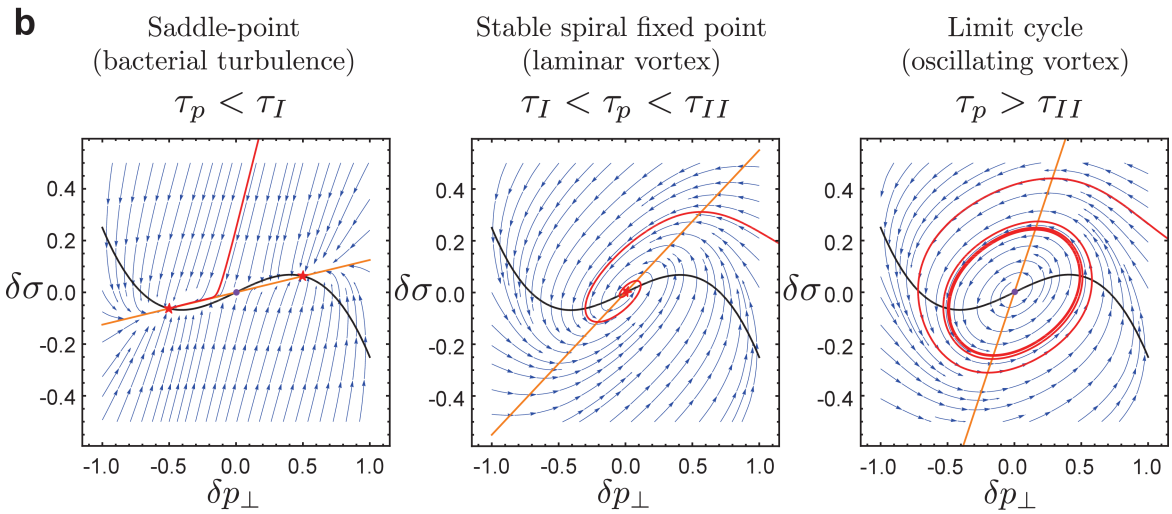

Extended Data Fig. 5 | Dynamical states and phase-space trajectories obtained from the theoretical model. a, The mode structure as a function of τ_p for fixed α, τ_R and $q \approx \sqrt{|\alpha|/K}$. For $\tau_p < \tau_I$, we have one purely real unstable mode ($\mathrm{Re}(\sigma) > 0$), while for $\tau_p > \tau_{II}$, the unstable modes have a finite frequency of oscillation. Here σ is the eigenvalue of the linear stability matrix. **b**, The phase-plane portraits in the $\{\delta p_\perp, \delta\sigma\}$ plane for the three different regimes $\tau_p < \tau_I$, $\tau_I < \tau_p < \tau_{II}$ and $\tau_p > \tau_{II}$. We have included the leading gradient-free nonlinear term $\delta p_\perp^3$ to saturate the polarization when unstable. This makes the system akin to the FitzHugh–Nagumo model for $\tau_p \gtrsim \tau_{II}$, leading to relaxation oscillations and excitability. The black and orange lines are the nullclines, and the red line is a representative trajectory that either converges to a fixed point or to a limit cycle. The red stars at the intersection of the nullclines are stable fixed points (or foci), while the blue dots are unstable fixed points (or foci). The labels to the three frames highlight the correspondence between the nature of the dynamical state obtained from the FitzHugh–Nagumo model and the states observed in experiments.

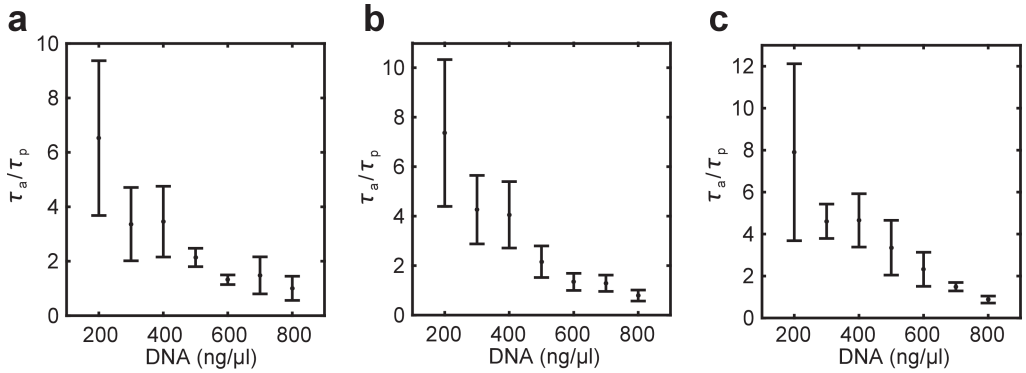

Extended Data Fig. 6 | Ratio between active shearing time and DNA relaxation time in giant vortices plotted against DNA concentration. **a**–**c**, The Maxwell relaxation time of DNA solutions τ_p was measured by microrheology (Methods). The active shearing timescale $\tau_a = \Gamma l_a^2/|\alpha| \approx K/\alpha^2$ in giant vortices cannot be computed precisely, as the relevant parameters are unknown. Instead, τ_a is estimated as the inverse of shear rate associated with bacterial collective motion, that is, the correlation length of collective velocity field divided by mean collective speed. Cell density was fixed at 4×10, 6×10 and 8×10 cells ml^{-1} for **a**, **b** and **c**, respectively. The mean and uncertainty of each data point in the plots were computed based on the data of τ_p and τ_a measured from at least three giant vortices. Overall, τ_p approaches τ_a when unidirectional vortices transit to an oscillatory state, a result qualitatively consistent with our active-matter model.

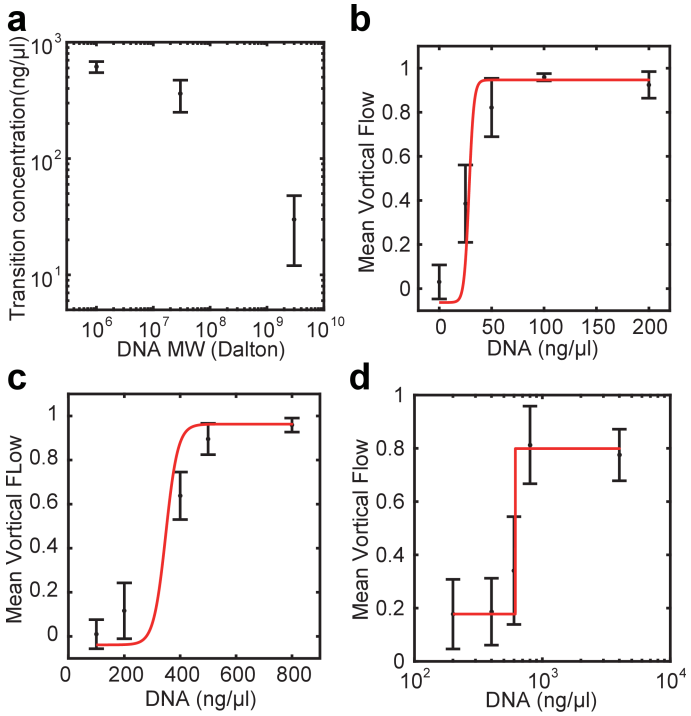

Extended Data Fig. 7 | High-molecular-weight DNA can give rise to giant vortices. a, DNA concentration threshold (d_1) for the transition from bacterial turbulence to unidirectional giant vortex decreases with molecular weight (N) for the three types of DNA tested (*E. coli* genomic DNA, lambda phage DNA, and salmon testes DNA; Methods). The transition DNA concentration threshold and its uncertainty (indicated by error bars) for different types of DNA molecules was estimated based on sigmoidal fit of the normalized mean vortical flow as a function of DNA concentration; see Methods. **b**–**d**, Normalized mean vortical flow of bacterial suspension drop versus *E. coli* DNA concentration obtained (**b**, *E. coli* genomic DNA, same as Extended Data Fig. 3b and replotted here for comparison; **c**, lambda phage DNA; **d**, salmon testes DNA). Error bars indicate standard deviation, $N \geq 4$. The data in these plots were obtained in the same way as in Extended Data Fig. 3b. The diameters of suspension drops were ~1.5 mm. Cell density was fixed at 6×10 cells ml^{-1}. See more discussion in Methods.

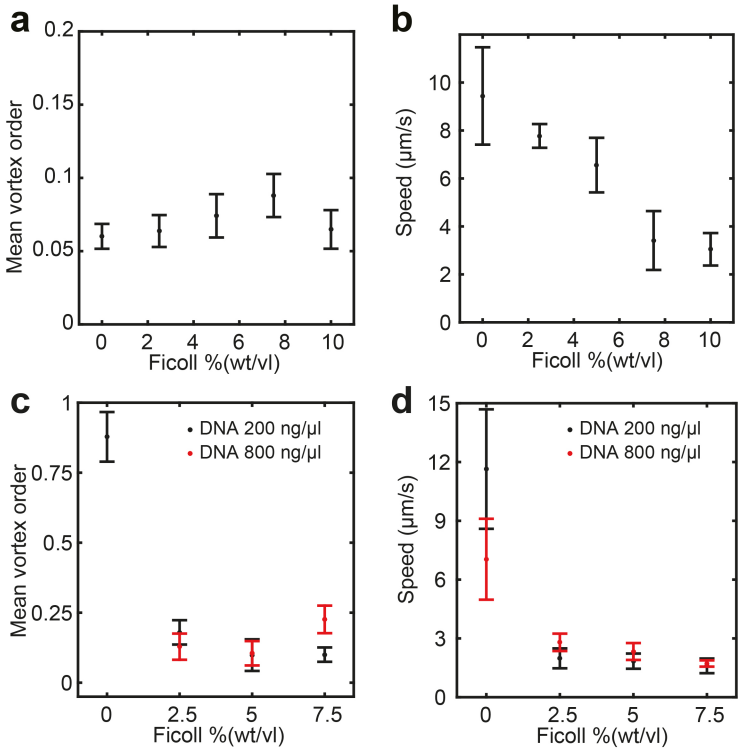

Extended Data Fig. 8 | Effect of viscosity on bacterial collective motion in suspension drops. The suspension drop diameter was ~1.5 mm. Cell density was fixed at 6×10 cells ml^{-1}. **a**, **b**, Mean vortex order and average collective speed of bacterial suspension drops without additive DNA plotted against Ficoll (Ficoll 400, molecular weight 400 kDa; Sigma catalogue number F9378) concentration. The mean vortex order of a specific suspension drop was computed as the time average of absolute instantaneous vortex order (that is, normalized mean vortical flow) over a time window of ~20 s. For a specific Ficoll concentration, the average collective speed of a suspension drop was computed as the time average of collective speed over a time window of ~20 s. **c**, **d**, Mean vortex order and average collective speed of bacterial suspension drops with additive DNA plotted against Ficoll concentration. Black (or red) colour indicates the experiments with *E. coli* genomic DNA concentration 200 (or 800) ng μl^{-1}, which normally supports the development of unidirectional or oscillatory giant vortices, respectively. Neither a stable unidirectional giant vortex nor an oscillatory giant vortex could be observed at all Ficoll concentrations (without additive DNA) or at Ficoll concentrations ≥2.5% (with DNA). Error bars in **a**–**d** indicate standard deviation ($N \geq 5$ suspension drops).

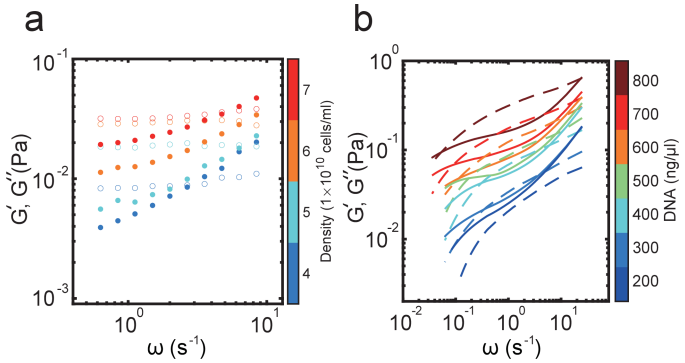

Extended Data Fig. 9 | Dynamic modulus of pure bacterial suspension and DNA solution. a, Dynamic modulus of pure bacterial suspension measured by a rheometer as a function of frequency (Methods), showing viscoelasticity consistent with the Kelvin–Voigt model. The measurement was made on the scale of ~100 μm, comparable to the length scale of bacterial collective motion. Open circles represent the storage modulus (G'); solid circles represent the loss modulus (G''). The colourmap indicates cell density. The elastic modulus of the bacterial suspension measured in the range of ~0.1–1 Hz was used to compute the data points in Fig. 4e. **b**, Dynamic modulus of DNA solution measured by microrheology (Methods). The dashed line represents the storage modulus (G'); the solid line represents the loss modulus (G''). The colourmap indicates the DNA concentration. The DNA solution behaves as a Maxwell material. Note that the viscosity η of DNA solutions obtained from our microrheology measurement is much higher than that of water (for example, $\eta \approx 0.106$ Pa s at DNA concentration 200 ng μl^{-1}; Methods). The fact that cells were able to swim at a normal speed of ~20–30 μm s^{-1} at the DNA concentrations tested here suggest that swimming bacteria induce a strong shear thinning effect in DNA solutions.

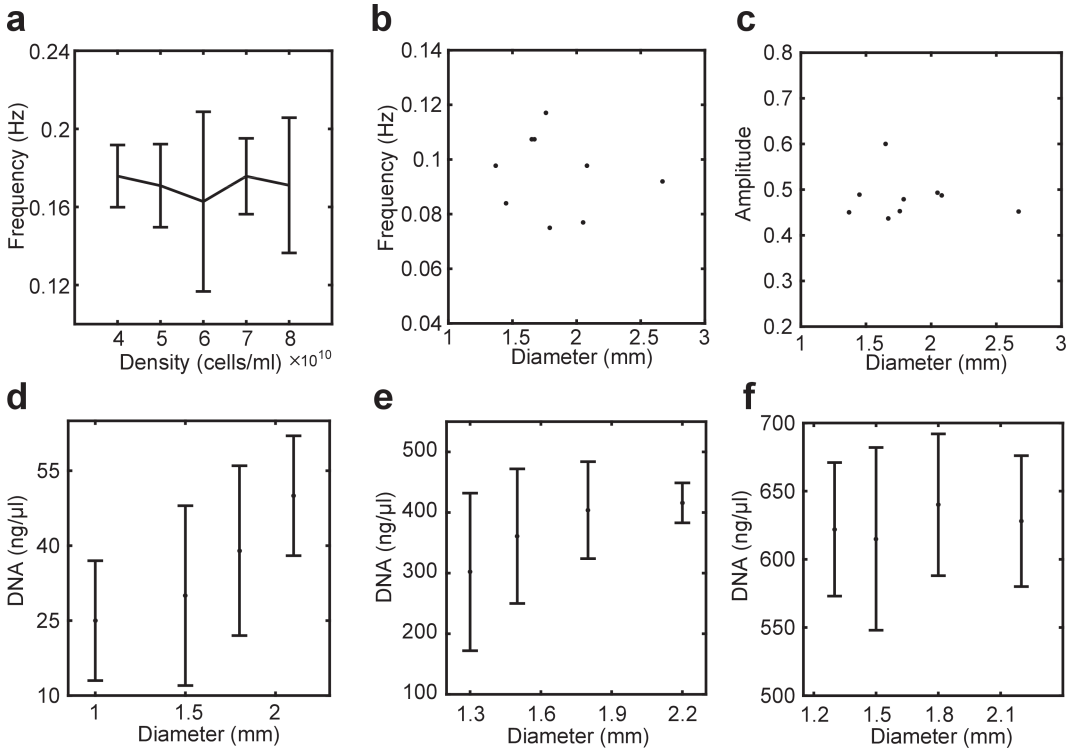

Extended Data Fig. 10 | Confinement effect on the development of giant vortex state. a, Without spatial confinement (for example, in centimetre-scale bacterial swarming colonies), dense bacterial active fluids can display collective oscillatory motion with the oscillation frequency independent of cell density as shown in the plot here (error bars indicate standard variation; $N = 5$). **b**, **c**, Oscillation frequency (**b**) and vortical flow amplitude (**c**) in oscillatory giant vortices plotted against confinement size (that is, diameter of suspension drops). Each dot in **b**, **c** represents the data from one suspension drop with the specified size. Cell density was fixed at ~6×10 cells ml^{-1} and *E. coli* genomic DNA concentration was fixed at ~300 ng μl^{-1}. **d**–**f**, DNA concentration threshold for the transition from bacterial turbulence to unidirectional giant vortex plotted against confinement size in the case of *E. coli* genomic DNA (**d**), lambda phage DNA (**e**) and salmon testes DNA (**f**). The DNA concentration threshold and its uncertainty (indicated by error bars) were estimated based on sigmoidal fit of normalized mean vortical flow as a function of DNA concentration (Methods). Cell density in **d**–**f** was fixed at ~6×10 cells ml^{-1}. Taken together, spatial confinement is necessary but not sufficient for giant vortex development; see more discussion in Methods.